Electronic Supplementary Material (ESI) for New Journal of Chemistry.

Flexible Self-poled Piezoelectric Nanogenerator Based on *r*GO-Ag/PVDF Nanocomposite

Manojit Pusty,[a] Lichchhavi Sinha,[a] and Parasharam M. Shirage [a,b,*]

[a]Discipline of Metallurgy Engineering and Materials Science, Indian Institute of Technology Indore, Simrol, Indore 453552, India

[b]Discipline of Physics, Indian Institute of Technology Indore, Simrol, Indore 453552, India

* Corresponding author E-mail: paras.shirage@gmail.com, pmshirage@iiti.ac.in.

Tel.: **+91-787-5222-331**

Crystallinity Calculation from XRD Measurements:

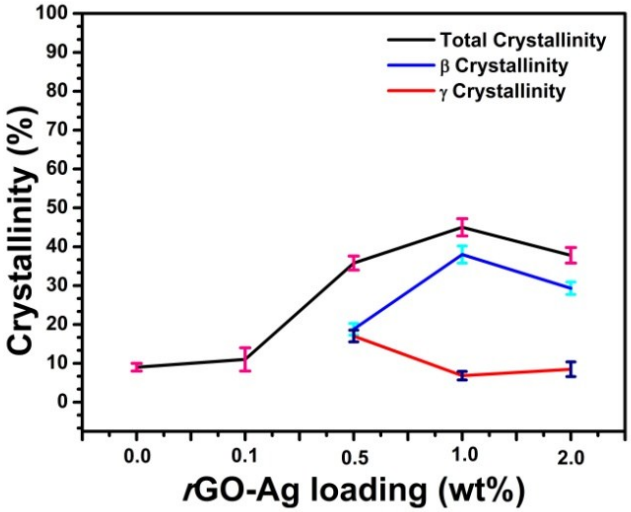

Fig. S1 The variation of total crystallinity, β crystallinity, and γ crystallinity in different loadings of *r*GO-Ag/PVDF.

The total degree of crystallinity was calculated from equation S1, where χ_{C_t} denotes total degree of crystallinity, A_{cr} is the integral area of the crystalline peaks and A_{amr} is the integral area of the amorphous peaks of PVDF.

$$\chi c_t = \frac{\sum A_{cr}}{\sum A_{cr} + \sum A_{amr}} \times 100\ \%$$

Equation S1

The percentage of β-crystallinity is found from equation S2, where χc_β is the total β-crystallinity, A_β is the integral area of the β crystalline peaks and A_γ is the integral area of the γ crystalline peaks. Similarly, the γ crystallinity is found from equation S3, where χc_γ indicates percentage of γ-crystallinity.

$$\chi c_\beta = \chi c_t \times \frac{\sum A_\beta}{\sum A_\beta + \sum A_\gamma}\ \%$$

Equation S2

$$\chi c_\gamma = \chi c_t \times \frac{\sum A_\gamma}{\sum A_\beta + \sum A_\gamma}\ \%$$

Equation S3

Calculation of relative proportion of electroactive polar phases:

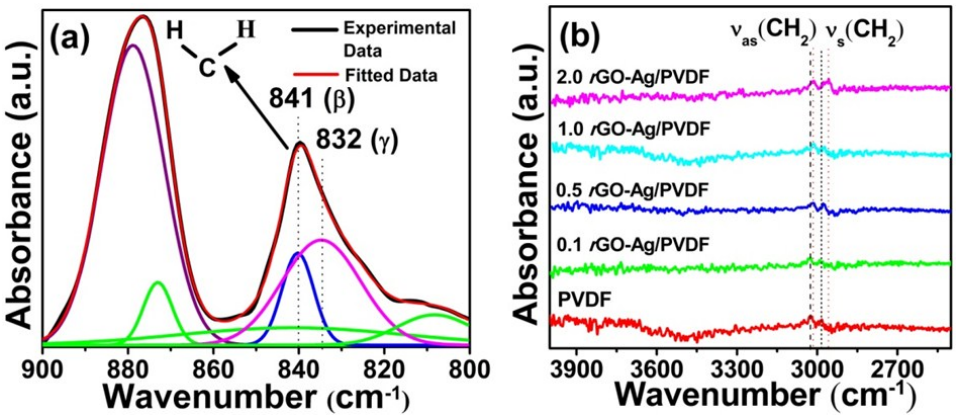

Fig. S2 (a) The deconvoluted FT-IR spectra of 1.0 *r*GO-Ag/PVDF nanocomposite film in the region of 900-800 cm^{-1} (b) the spectra of all the PVDF films in the region of 4000-2500 cm^{-1}.

It can be noticed in Fig. S2 (a) from the deconvoluted FT-IR spectra that the peak at 841 cm^{-1} which originates because of $–CH_2–$ wagging vibrations belongs to the β- phase which exists beside the 832 cm^{-1} peak belonging to the γ phase.

Fig. S2 (b) shows the FT-IR spectra between 4000 cm^{-1} and 2500 cm^{-1} where it can be seen that the two fundamental vibrational bands for $\nu_{as}(–CH_2–)$ and $\nu_s(–CH_2–)$ were shifted to a lower frequency region which indicates the presence of interfacial interaction between the surface charge of *r*GO-Ag and $–CH_2/CF_2–$ dipoles of the PVDF based nanocomposite. These results confirm that *r*GO-Ag plays a vital role in the formation of the γ-phase. Electrostatic interaction of *r*GO-Ag with the $–CH_2–/–CF_2–$ dipoles present in PVDF plays a role in this phenomenon. The electrostatic interactions originate not only from the charges present at the surface due to Ag but also due to the delocalized π electrons along with the oxygen-containing functional groups present in *r*GO. The presence of the positive charges in *r*GO-Ag sheets leads to the interaction with $–CF_2–$ dipoles of the PVDF segments which helps the formation and stabilization of the polar β- and γ-phase.

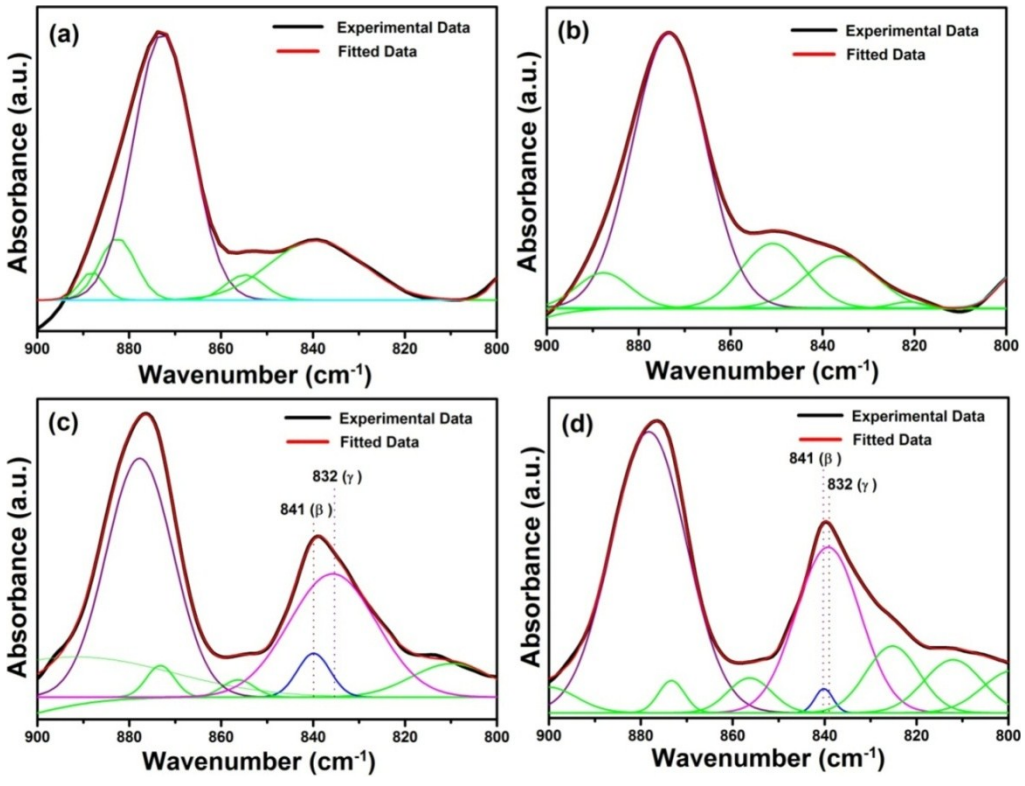

Fig. S3 The Deconvoluted FT-IR spectra of (a) PVDF, (b) 0.1 *r*GO-Ag/PVDF, (c) 0.5 *r*GO-Ag/PVDF, (d) 2.0 *r*GO-Ag/PVDF.

The deconvoluted FT-IR spectra of PVDF, 0.1 *r*GO-Ag/PVDF, 0.5 *r*GO-Ag/PVDF, 2.0 *r*GO-Ag/PVDF are shown in Fig. S3a, b, c, d respectively. A shift in the deconvoluted peaks corresponding to the β- and γ-phase is observed in 0.5 and 2.0 *r*GO-Ag/PVDF, which can be attributed to the change in the interaction of *r*GO-Ag with PVDF chains as the filler loading increases.

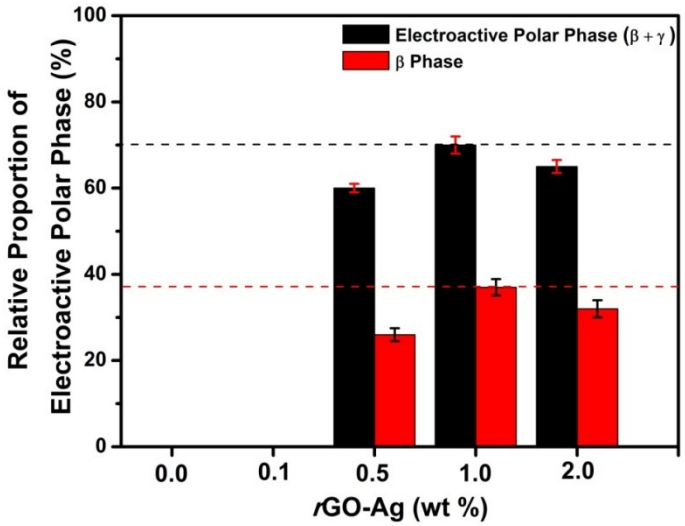

Fig. S4 Variation of relative proportion in percentage of electroactive polar both β- and γ-phases (in black) and only β- phases (in red).

The relative proportion of polar electroactive phases (both β and γ) denoted by F (β,γ) present in *r*GO-Ag/PVDF is calculated from the following equation:

$$F(\beta,\gamma) = \frac{A_{(841)}}{\left(K_{(841)}/K_{(832)}\right)A_{(832)} + A_{(841)}}$$

Equation S4

where A_{841} and A_{832} is the absorption intensity at 841 cm^{-1} and 832 cm^{-1} respectively whereas K_{841} and K_{832} is the absorption coefficient at 841 cm^{-1} and 832 cm^{-1} respectively.

The relative proportion of individual presence of β phase is denoted by F_β and the individual presence of γ phase is denoted by F_γ.

$$F_\beta = F(\beta,\gamma) \times \frac{A_\beta}{A_\beta + A_\gamma} \times 100\% \quad \textbf{Equation S5}$$

$$F_\gamma = F(\beta,\gamma) \times \frac{A_\gamma}{A_\beta + A_\gamma} \times 100\% \quad \textbf{Equation S6}$$

where A_γ and A_β are the integrated areas under the γ and β deconvoluted curves.

The $F(\beta,\gamma)$ was found to be 70 % whereas F_β was calculated to be 38 % in case of 1.0 *r*GO-Ag/PVDF which was highest among all the *r*GO-Ag/PVDF nanocomposite loadings, which is shown in Figure S4.

A_{841} and A_{832} are the absorption intensities at 841 cm^{-1} and 832 cm^{-1} respectively. K_{841} and K_{832} are the absorption coefficients at the respective wavenumbers.

Measurement of Damping Coefficient:

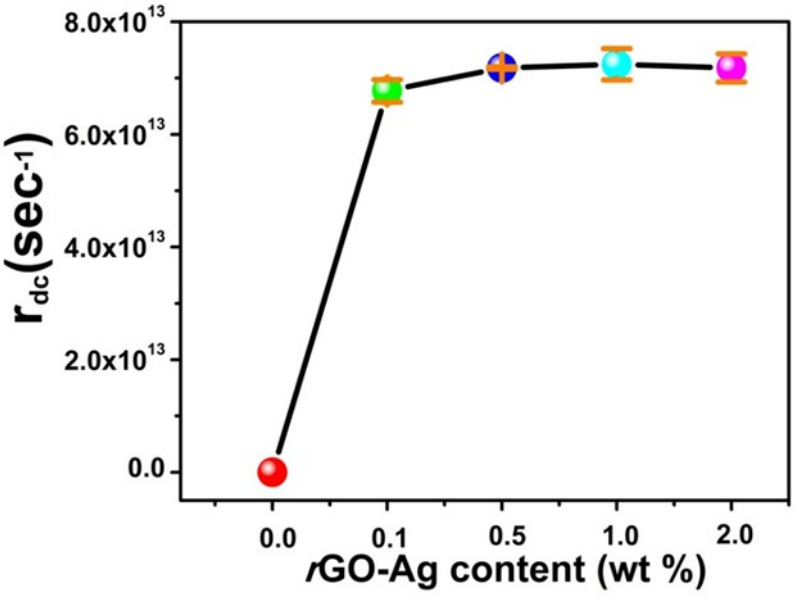

Fig. S5 Variation of the damping coefficient with the increase in the filler concentration loading.

The variation of damping coefficient with the rise in the addition of *r*GO-Ag concentration is shown in Fig. S5. The damping coefficient is an important tool to ascertain the interaction between *r*GO-Ag nanosheets and PVDF chains. The asymmetric $\nu_{as}(–CH_2–)$ and symmetric $\nu_s(–CH_2–)$ stretching vibration bands of PVDF existing in the region between 3060 to 2940 cm^{-1} do not overlap with other vibrational bands. However, $\nu_{as}(–CH_2–)$ and $\nu_s(–CH_2–)$ vibrational bands shift towards lower wavenumber with the increase in *r*GO-Ag filler concentration due to the damping oscillations of the $–CH_2–$ dipoles, which is shown in Fig. S6. The overall mass of the $–CH_2–$ dipoles of the PVDF increases because of the electrostatic interactions between the $–CH_2–$ dipoles and surface charge of *r*GO-Ag. The damping coefficient increases with 1 weight percentage loading; however, it decreases slightly at 2 weight percentage *r*GO-Ag filler loading.

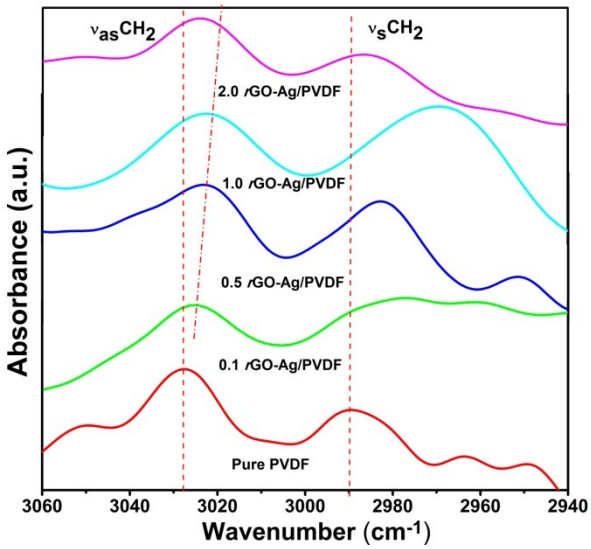

Fig. S6 FT-IR spectra of the PVDF based nanocomposite with different *r*GO-Ag loadings in the region of 3060-2940 cm^{-1}.

The damping coefficient (r_{dc}) is calculated by using the following formula:

$$r_{dc} = 4\pi c(\bar{\nu}^{2}_{PVDF} - \bar{\nu}^{2}_{rGO-Ag/PVDF})^{1/2}$$ **Equation S7**

where c is the velocity of light, $\bar{\nu}^{2}_{PVDF}$ is the wavenumber of damping free oscillation of the $-CH_2-$ group in pure PVDF, whereas $\bar{\nu}^{2}_{rGO-Ag/PVDF}$ is the damping originating from the $-CH_2-$ groups in *r*GO-Ag/PVDF nanocomposite.

Measurement of Dichroic Ratio:

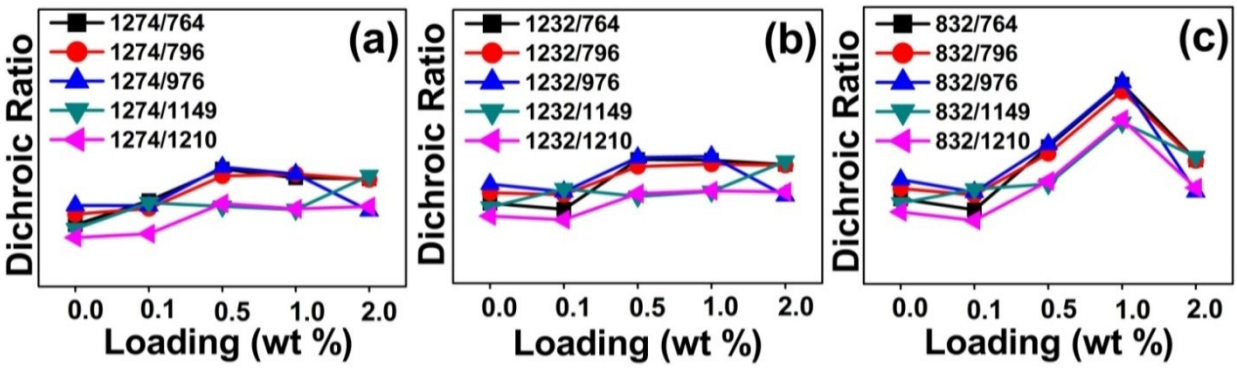

Figure S7. Dichroic ratio of the peak present at (a) 1274 cm^{-1} belonging to β-phase, (b) 1232 cm^{-1} belonging to γ-phase and (c) 832 cm^{-1} belonging to γ-phase.

The dichroic ratio is also another means to quantitatively analyze the crystal structures present in the nanocomposite films. The dichroic ratio is obtained by dividing the intensity of

crystalline polar phases with the intensities of all the α-phase peaks present, in the FT-IR spectra, as shown in Fig. 2 in the main text. Fig. S7a shows the dichroic ratio obtained by dividing the intensity of the 1274 cm^{-1} peak belonging to the crystalline β-phase with that of the intensities of all the α-phase peaks present at 764, 796, 976, 1149, 1210 cm^{-1}. Fig. S7b shows the dichroic ratio obtained by dividing the peak intensities of γ-phase present at 1232 cm^{-1} with the intensities of all the α-phase peaks present. Fig. S7c shows the dichroic ratio obtained between the intensity of the 832 cm^{-1} peak belonging to polar electroactive phases (contributed by both β- and γ-phases), as shown in the peak deconvolution in Fig. S2a and intensities of all the α-phase peaks. The relative amount of the electroactive polar phases increases till 1 weight percentage filler loading. This indicates that the addition of *r*GO-Ag contributes in inducing the electroactive polar phases in PVDF. However, the dichroic ratio falls at 2 weight percentage of *r*GO-Ag filler loading. These results indicate firmly that the content of *r*GO-Ag contributes to the process of transformation of α-phase to polar (β- and γ-) electroactive phases. It is noteworthy here that in this work the variation of the dichroic ratio is observed without any external mechanical or electrical treatment to the PVDF nanocomposite films. [S1]

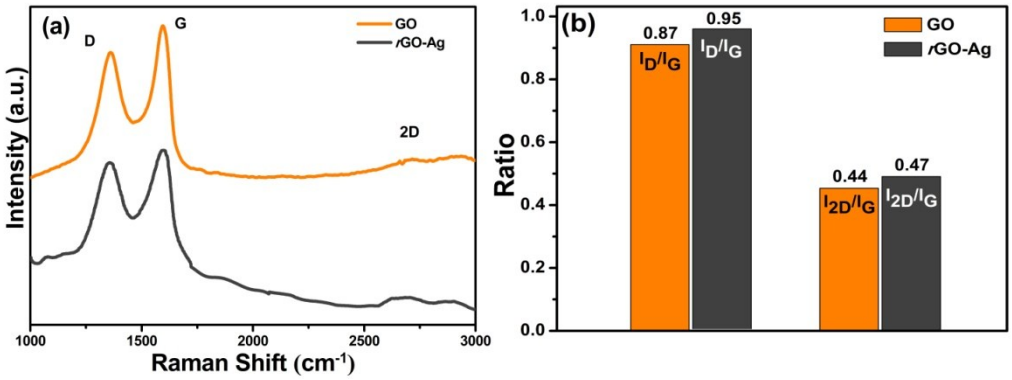

Fig. S8 Raman Spectra of (a) GO and *r*GO-Ag, (b) I_D/I_G and I_{2D}/I_G ratio of GO and *r*GO-Ag.

The Raman Spectra of GO and *r*GO-Ag is shown in Fig. S8a. In case of GO, the D band is located at 1361 cm^{-1} and is related to the size of the in-plane sp^2 domains. The G band is located near 1596 cm^{-1} which originate from the first order scattering of the E_2g phonons of

the sp^2-hybridized carbon atoms. The 2D band originates at 2700 cm^{-1} which is sensitive to the stacking of graphene sheets. The D band of *r*GO-Ag is located at 1356 cm^{-1}, the G band is located at 1600 cm^{-1} and the 2D band is located at 2682 cm^{-1}. The I_D/I_G and the I_{2D}/I_G ratio is shown in Fig. S8b. The I_D/I_G peak intensity ratio is a measure of the sp^2 domain size of graphene sheets containing sp^3 and sp^2 bonds and is inversely proportional to the average size of the sp^2 clusters. The I_D/I_G peak ratio of GO and *r*GO-Ag is 0.87 and 0.95 respectively. The I_D/I_G peak ratio in case of *r*GO-Ag increases, which indicates a reduction in the size of the sp^2 clusters in the reduction process. The I_{2D}/I_G peak ratio indicates the number of layers of graphene sheets present. The 2D/G ratio in case of GO and *r*GO-Ag is 0.44 and 0.47 respectively. It is reported that the ratio between the I_{2D}/I_G of single, double, triple and multi (>4) layered graphene sheets are typically greater than 1.6, ~0.8, ~0.30, and ~0.07 respectively. [S2] This indicates that triple layer graphene sheets are present in both GO and *r*GO-Ag. This result also concludes that during the reduction process of GO to *r*GO-Ag no significant amount of stacking of graphene sheets occurs.

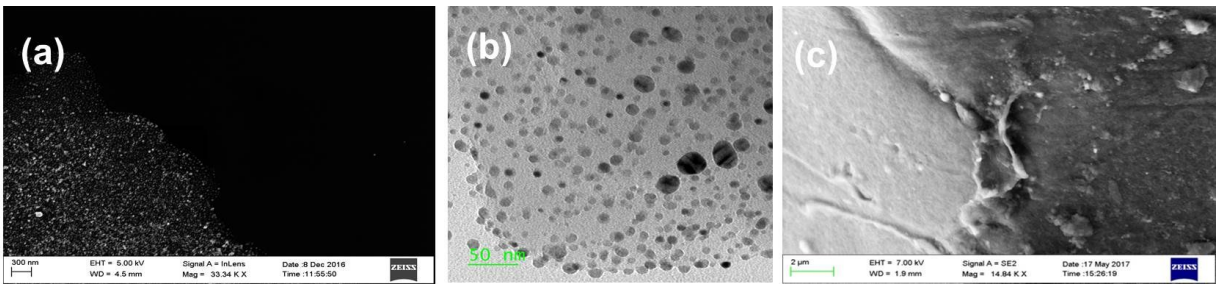

Fig. S9 (a) SEM image and (b) HRTEM image of *r*GO-Ag showing Ag nanoparticles embedded in a thin layer of *r*GO matrix, (c) SEM image of the surface morphology of 1.0 *r*GO-Ag/PVDF nanocomposite.

The Field emission scanning electron microscopy (FE-SEM) image of the *r*GO-Ag nanocomposite is shown in Fig. S9a which shows the presence of layer-like *r*GO, within

which silver nanoparticles are evenly dispersed. From the transmission electron microscopy (TEM) image as shown in Fig. S9b the average particle size of the silver nanoparticles (Ag-NP) can be calculated to be between ≈20 and ≈30 nm. The Ag NPs are evenly dispersed in the *r*GO matrix and contributes in the creation of conduction paths to bring the piezoelectric charges to the electrodes present in the top and the bottom electrodes which in turn increases the sensitivity of the nanocomposite.

Field Emission-Scanning Electron Microscopy was also conducted on the surface of 1.0 *r*GO-Ag/PVDF nanocomposite film to study the surface morphology. Fig. S9c shows wrinkled and crumbled morphology of the graphene sheets which are encapsulated by the PVDF polymer matrix. The encapsulation of the graphene sheets by the polymer visually confirms the bonding interactions between the polymer and the nanofiller.

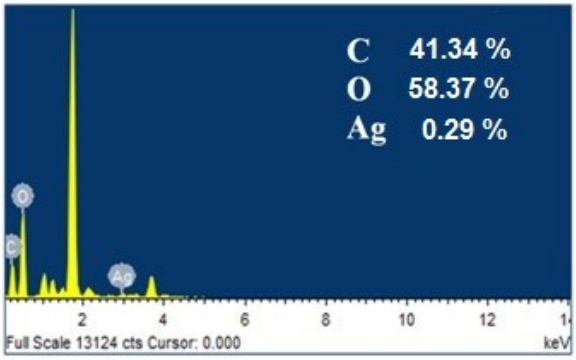

Fig. S10 EDS spectra of *r*GO-Ag, under HR-TEM study.

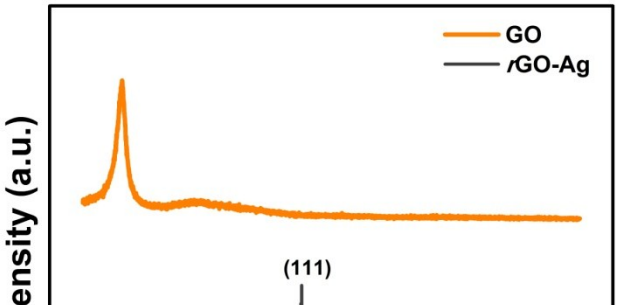

Fig. S11 XRD spectra of GO and *r*GO-Ag.

In the XRD spectra of *r*GO-Ag is shown in Fig. S11, a small hump at 25° indicates the exfoliation of Graphene layers from GO to form reduced graphene oxide. Also the peaks at 38.1°, 44.2°, 64.3°, 77.3° belongs to (111), (200), (220), (311) lattice planes of Ag nanoparticles belonging to the face-centred cubic structure.[S3]

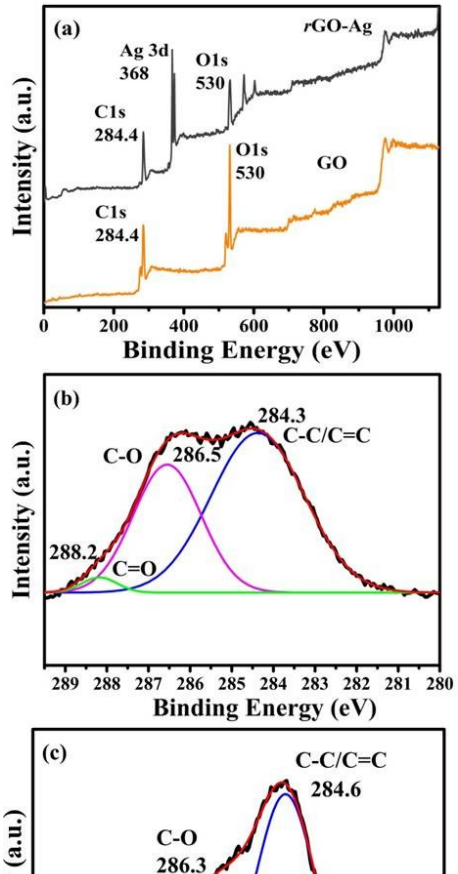

Fig. S12 (a) XPS Survey Spectra of GO and *r*GO-Ag, (b) C1s spectra of GO and (c) C1s spectra of *r*GO-Ag.

Fig. S12 (a) shows the XPS survey spectra of GO and *r*GO-Ag. The peak at 368 eV in the survey spectra of *r*GO-Ag belongs to Ag, which confirms the presence of metallic Ag in *r*GO-Ag. Fig. S12 (b) shows the C1s spectra of GO, where the peaks indicate the presence of C=C, C-O, C=O functional groups present in graphene oxide. Fig. S12 (c) shows the C1s spectra of *r*GO-Ag where a reduction in the intensity of the peaks of C-O and C=O is evident, which indicates the reduction of graphene oxide in the process of the formation of *r*GO-Ag.

Polarization-Electric Field Characterization:

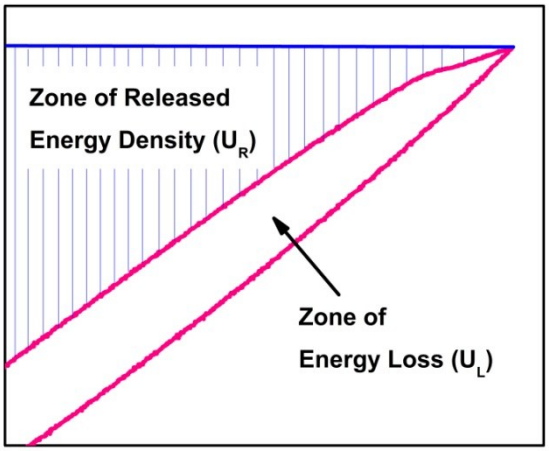

Fig. S13 Shaded area (blue bars) shows the zone of Released Energy Density (U_R) whereas area inside the PE-loop shows the zone of Energy Loss (U_L).

To calculate the efficiency of the nanocomposites the area under the zone of Released Energy Density (U_R) and the area under the zone of Energy Loss is calculated (U_L).

Electrical Characterizations:

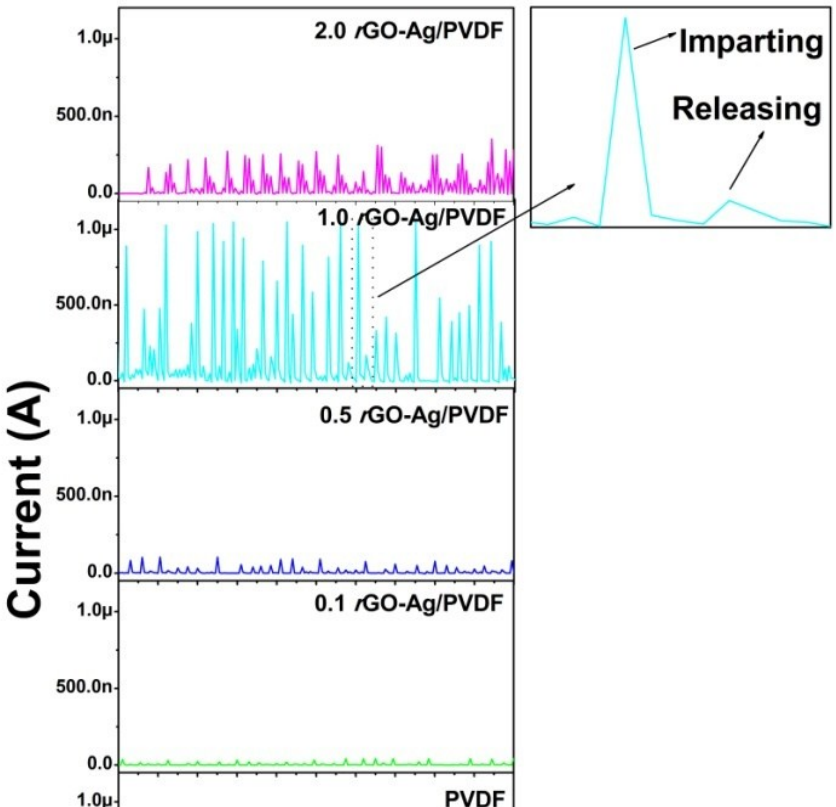

Fig. S14. The (a) rectified short-circuit current generated by the 2.0 *r*GO-Ag/PVDF, 1.0 *r*GO-Ag/PVDF, 0.5 *r*GO-Ag/PVDF, 0.1 *r*GO-Ag/PVDF, PVDF nanocomposite films upon human palm impulse imparting, (b) magnified image of one cycle of current response due to human palm impulse imparting and releasing action.

The rectified short-circuit current generated by the different loadings of *r*GO-Ag/PVDF nanocomposites are shown in Fig. S14a. The current detected from the 1.0 *r*GO-Ag/PVDF nanocomposite reached a maximum value of ~1.05 μA, whereas the current from the pure PVDF nanocomposite reached a maximum value of ~0.023 μA. It can be concluded that there is an increasing trend of current till 1 percentage weight loading of *r*GO-Ag, thereafter at 2 percentage weight loading it decreased. Fig. S14b shows the magnified view of a single cycle of the rectified short-circuit current.

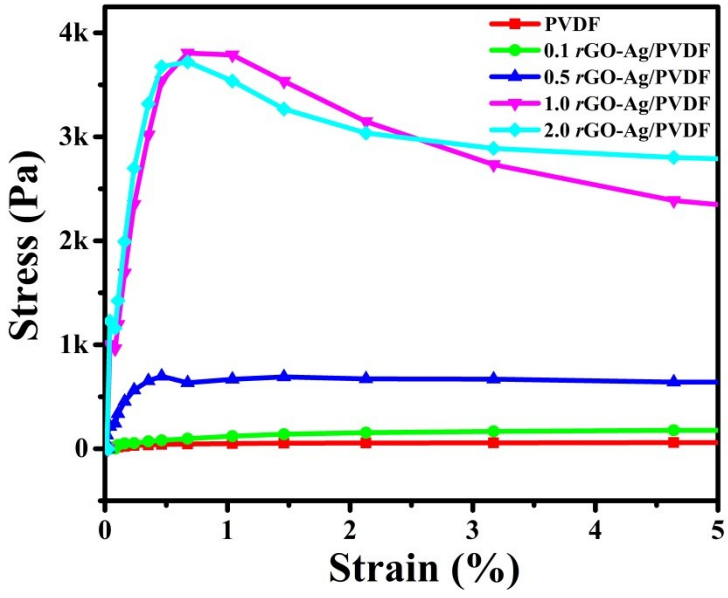

Fig. S15 Shows the Stress vs Strain curve of the *r*GO-Ag/PVDF nanocomposite with different filler loadings.

The Stress vs Strain curve for all the nanocomposites are shown in Fig. S15. The Young's Modulus of the 1.0 *r*GO-Ag/PVDF nanocomposite is found out to be 7.533 kPa, from the Stress vs Strain Curve.

Calculation of Imparted Pressure (σ)

The pressure imparted on the HPNG is calculated from the following equations:

$$m.g.h = \frac{1}{2} m.v^2 \quad \textbf{Equation S8}$$

$$(F - m.g).\Delta t = m.v \quad \textbf{Equation S9}$$

$$\sigma = \frac{F}{S} \quad \textbf{Equation S10}$$

Where m is the mass (the magnitude of mass shown in digital weigh balance by human palm striking which is equal to 0.400 kilograms), g= 9.8 N/kg, h= 0.3 m, Δt= 0.528 s (which is the average time between two voltage spikes), F is the force applied on the HPNG, σ is the stress applied on the PNG, S is the surface area of the electrodes.

The force applied on the HPNG was found out to be ≈ 6 N, and applied stress σ ≈ 4.6 kPa.

Energy Efficiency Calculation

The energy harvesting efficiency of the PNG during capacitor charging is given in Equation 7. The input energy (W_{in}) provided to the PNG while charging the capacitor during one cycle is given by

$$W_{in} = F \times \Delta l = F \frac{\sigma l}{Y} = 36 \times 10^{-6}\ J \quad \textbf{Equation S11}$$

Where F is (6 N) which is the applied force on 1.0 *r*GO-Ag/PVDF based PNG, Δl is the deformation of the PNG when stress σ (4.6 kPa) is applied and Y is the Young's Modulus

(7.533 kPa) of the nanocomposite and the average thickness of the nanocomposite film *l* is 0.01 mm.

The total input mechanical energy transfer to the PNG during the capacitor charging is given by

$$E_{in} = \frac{t}{\Delta t} W_{in} = 0.0375 \text{ J} \quad \textbf{Equation S12}$$

where *t* is the total time required to charge the capacitor, which is 550 s. Δt is the average time duration between the two consecutive voltage peaks of the imparting pressure cycles, which is 0.528 s.

$$E_{out} = \frac{1}{2} CV^2 = 245 \times 10^{-6} \text{ J} \quad \textbf{Equation S13}$$

The overall energy efficiency (η) can be found out from the ratio of the electrical energy stored (E_{out}= ½ CV^2) in the 10 μf capacitor while charging and the total mechanical energy used (E_{in}) to charge the 10 μf capacitor.

$$\eta = \frac{E_{out}}{E_{in}} \times 100\ \% = 0.65\ \% \quad \textbf{Equation S14}$$

Table S1: Performance details of previously reported data on energy harvesting devices

Sl. No.	Name of the Piezoelectric Device	Poling Voltage and Duration	Input Source	Voltage (V)	Current (I)
1	Cellulose-ZnO[S4]	Data	Ultrasonic bath	80 mV	1.25 μA

		Unavailable			
2	ZnO NWs/PVDF[S5]	100 kV/mm	Linear motor	0.2 V	10 nA/cm^2
3	Li doped ZnO NW-Polymer Composite[S6]	105 kV/cm; 20 h	Bending stage	180 V	50 µA
4	$BaTiO_3$ NPs[S7]	100 kV/cm; 20 h	Bending stage	3.2V	350 nA
5	$ZnSnO_3$[S8]	Not Found	Human finger press	40 V	0.4 µA
6	$KNbO_3$ Nanorod[S9]	150 kV; 1h	Linear motor	3.2 V	67.5 nA
7	$KNbO_3$ Nanowires[S10]	5.0 kV/mm; 1 h	Bending tester	10.5 V	1.3 µA
8	$BaTiO_3$ Nanotubes[S11]	80 kV/cm; 12 h	Linear motor	5.5 V	350 nA
9	KNN-LTS[S12]	2 KV/mm; 24 h	Mechanical tapping	53 V	15 µA
10	Native Cellulose microfiber[S13]	Not Poled	Human hand punching	30 V	500 nA
11	PVDF/AlO-*r*GO[S14]	Not Poled	Human hand punching	36 V	0.8 µA
12	BCTZ NPs–polymer composite[S15]	1.5 kV: Data Unavailable	Bending stage	15 V	0.8 µA
13	PVDF-TrFE Film/Graphene Oxide[S16]	30 MV/m, 1 h	Hydraulic/Mechanical fatigue tester	4.3 V	1.88 µA
14	GAg/PVDF[S17]	Not Poled	Mechanical stepper machine	100mV	0.1 nA
15	Fe-RGO/PVDF[S18]	Not Poled	Human hand punching	5.1 V	0.254 µA
16	Fe-RGO/PVDF[S19]	Not Poled	Human Finger Tapping	1.2 V	342 nA
17	CNT/PVDF[S19]	Not Poled	Human Finger Tapping	2.5 V	680 nA
18	*r*GO-Ag/PVDF **(Present Work)**	Not Poled	Human hand punching	18 V	1.05 µA

References

S1. Alamusi, J. M. Xue, L. K. Wu, N. Hu, J. Qiu, C. Chang, S. Atobe, H. Fukunaga, T. Watanabe, Y. L. Liu, H. M. Ning, J. H. Li, Y. Li and Y. Zhao, *Nanoscale,* 2012, **4**, 7250-7255.

S2. O. Akhavan, *Carbon,* 2015, **81**, 158-166.

S3. M. Pusty, A. K. Rana, Y. Kumar, V. Sathe, S. Sen and P. Shirage, *ChemistrySelect,* 2016, **1(14),** 4235-4245.

S4. A. Kumar, H. Gullapalli, K. Balakrishnan, A. B. Mendez, R. Vajtai, M. Terrones and P. M. Ajayan, *Small,* 2011, **7***,* 2173-2178.

S5. Q. Liao, Z. Zhang, X. Zhang, M. Mohr, Y. Zhang and H. J. Fecht, *Nano Research,* 2014, **7(6)**, 917-928.

S6. S. H. Shin, Y. H. Kim, M. H. Lee, J. Y. Jung, J. H. Seol and J. Nah, *ACS Nano,* 2014, **8(10)**, 10844-10850.

S7. K. I. Park, M. Lee, Y. Liu, S. Moon, G. T. Hwang, G. Zhu, J. E. Kim, S. O. Kim, D. K Kim, Z. L. Wang and K. J. Lee, *Adv. Mater.,* 2012, **24**, 2999-3004.

S8. M. M. Alam, S. K. Ghosh, A. Sultana and D. Mandal, *Nanotechnology,* 2015, **26**, 165403-165408.

S9. J. H. Jung, C. Y. Chen, B. K. Yun, N. Lee, Y. Zhou, W. Jo, L. J. Chou and Z. L. Wang, *Nanotechnology,* 2012, **23**, 375401-375406.

S10. M. R. Joung, H. Xu, I. T. Seo, D. H. Kim, J. Hur, S. Nahm, C. Y. Kang, S. J. Yoon and H. M. Park, *J. Mater. Chem. A,* 2014, **2**, 18547-18553.

S11. Z. H. Lin, Y. Yang, J. M. Wu, Y. Liu, F. Zhang and Z. L. Wang, *J. Phys. Chem. Lett*., 2012, **3**, 3599-3604.

S12. Q. T. Xue, Z. Wang, H. Tian, Y. Huan, Q. Y. Xie, Y. Yang, D. Xie, C. Li, Y. Shu and X. H. Wang, T. L. *AIP Adv.,* 2015, **5**, 017102-017108.

S13. M. M. Alam and D. Mandal, *ACS Appl. Mater. Interfaces,* 2016, **8**, 1555-1558.

S14. S. K. Karan, R. Bera, S. Paria, A. K. Das, S. Maiti, A. Maitra and B. B. Khatua, *Adv. Energy Mater.,* 2016, **6**, 1601016-1601027.

S15. C. Baek, J. H. Yun, J. E. Wang, C. K. Jeong, K. J. Lee, K. I. Park and D. K. Kim, *Nanoscale,* 2016, **8**, 17632-17638.

S16. V. Bhavanasi, V. Kumar, K. Parida, J. Wang and P. S. Lee, *ACS Appl. Mater. Interfaces,* 2016, **8**, 521-529.

S17. T. K. Sinha, S. K. Ghosh, R. Maiti, S. Jana, B. Adhikari, D. Mandal and S. K. Ray, *ACS Appl. Mater. Interfaces,* 2016, **8**, 14986-14993.

S18. S. K. Karan, D. Mandal and B. B. Khatua, *Nanoscale,* 2015, **7**, 10655-10666.

S19. M. Pusty, A. Sharma, L. Sinha, A. Chaudhary and P. Shirage, *ChemistrySelect,* 2017, **2(9)**, 2774-2782.